Constraints on early Mars atmospheric pressure inferred from small ancient craters

Edwin S. Kite[1], Jean-Pierre Williams[2], Antoine Lucas[1], and Oded Aharonson[1, 3]

[1] *Geological and Planetary Sciences, Caltech.*

[2] *Earth and Space Sciences. University of California - Los Angeles.*

[3] *Helen Kimmel Center for Planetary Science, Weizmann Institute of Science, Israel.*

The single most important control on long-term climate change on Mars is thought to be decay of the CO_2-dominated atmosphere, but direct constraints on paleoatmospheric pressure *P* are lacking. Of particular interest is the climate that allowed rivers to flow early in Mars history, which was affected by *P* via direct and indirect greenhouse effects. The size of craters embedded within ancient layered sediments is a proxy for *P*: the smaller the smallest craters that form, the thinner the past atmosphere. Here we use high-resolution orthophotos and Digital Terrain Models (DTMs) to identify embedded craters among the river deposits of Aeolis Dorsa, and compare their sizes to models of atmospheric filtering of impactors by thicker atmospheres. The best fit is $P \leq 760 \pm 70$ mbar, rising to $P \leq 1640 \pm 180$ mbar if rimmed circular mesas are excluded. Surveys tend to undercount smaller craters, so these fits are upper limits. Our work assumes target properties appropriate for desert alluvium: if sediment developed bedrock-like rock-mass strength by early diagenesis, the upper limit is greatly increased. If Mars did not have a stable multibar atmosphere at the time that the rivers were flowing, the warm-wet CO_2 greenhouse of Pollack et al. (1987) is ruled out, and long-term average temperatures were probably below freezing.

Planetary atmospheres brake, ablate, and disrupt small asteroids and comets, filtering out small hypervelocity surface impacts and causing fireballs, airblasts, meteors, and meteorites. The 2013 Chelyabinsk airburst exemplifies atmospheric destruction of an object that would create a $D >$ 100 m crater in the absence of an atmosphere. The smallest hypervelocity craters near sea-level on Earth have $D \sim 20$ m. "Zap pits" as small as 30 μm are known from the airless Moon, but other

worlds show the effects of progressively thicker atmospheres: the modern Mars atmosphere is capable of removing >90% of the kinetic energy of >240 kg impactors (Chappelow & Golombek, 2010); Titan's paucity of small craters is consistent with a model predicting atmospheric filtering of craters smaller than 6-8 km (e.g. Wood et al., 2010); and on Venus, craters $D < 20$ km are substantially depleted by atmospheric effects (Herrick et al., 1997).

Changes in the concentration of atmospheric volatiles are believed to be the single most important control on Mars climate evolution and habitability. Contrary to early work (Pollack, 1987), it is doubtful that increasing CO_2 pressure (≈total atmospheric pressure, P) is enough to raise early Mars mean-annual surface temperature ($\overline{T}$) to the freezing point, even when water vapor and cloud feedbacks are taken into account (Forget et al., 2012). However, increased CO_2 aids transient surface liquid water production by impacts, volcanism, or infrequent orbital conditions (e.g., Tian et al., 2010; Kite et al., 2013a). Existing data requires an early epoch of massive atmospheric loss to space; suggests that the present-day rate of escape to space is small; and offers evidence for only limited carbonate formation (e.g., Barabash et al., 2007; Ehlmann, 2008). These data have not led to convergence among atmosphere evolution models, which must balance poorly understood fluxes from volcanic degassing, escape to space, weathering, and photolysis (e.g. Manning et al. 2006). More direct measurements (Manga et al., 2012) are required to determine the history of Mars' atmosphere. Wind erosion exposes ancient cratered volumes on Mars, and the size of exhumed craters has been previously suggested as a proxy of ancient Mars P (e.g., Vasavada et al., 1993).

Here we obtain a new upper limit on early Mars atmospheric pressure from the size-frequency distribution of small ancient craters interspersed with river deposits in Aeolis, validated using High Resolution Imaging Science Experiment (HiRISE) DTMs, in combination with Monte Carlo simulations of the effect of P on the crater flux. The craters are interbedded with river deposits up to ~10^3 km long, with inferred peak river discharge 10-1000 m^3/s (Burr et al., 2010). Therefore, the atmospheric state they record corresponds to an era when Mars was substantially wetter than the present, probably > 3.7 Ga (Supplementary Material).

Data

Aeolis Dorsa is a promising location to hunt for embedded craters: the stratigraphy is shot through with the deposits of large rivers, and when these overlie a crater, that crater must be as ancient as the rivers (Kite et al., 2013b). Beds near the base of one particularly well-preserved fluvial unit in Aeolis Dorsa (Supplementary Material) preserve a high density of ancient craters, perhaps due to slow deposition or material properties unusually favorable for crater preservation. We constructed stereo DTMs/orthophotos for two stereo image-pairs covering these beds, DTM1 and DTM2 (as described in the Methods). Following a checklist (Supplementary Text), craters were classified as definite ancient craters (visibly embedded within stratigraphy: e.g., overlain by river deposit) (n = 56, median diameter D_{50} = 107 m, 10th-percentile diameter D_{10} = 50 m), rimmed circular mesas (RCM) (n = 71, D_{50} = 48 m, D_{10} = 21 m), or candidate ancient crater (n = 192, D_{50} also 48 m, D_{10} also 21 m; candidates are not considered further, but their inclusion would strengthen our conclusions). We measured D by fitting circles to preserved edges/rims. RCM appear as disks in raw HiRISE images. We interpret them as the erosionally-resistant fills (or erosionally-resistant floors) of impact craters that have become inverted during the deflation of the target unit. They are unlikely to be outliers of a young mantle because they are not found away from the fluvial unit (Supplementary Text). We plot them separately, but consider them to be probable ancient craters. We used unambiguously ancient craters as a guide to the preservation state of the smaller craters. These ancient craters are unlikely to be maars, because maars are not randomly distributed in space or time/stratigraphy. We also reject the possibility that they are paleo-karst sinkholes, because sinkholes lack rims, are concentrated at particular stratigraphic levels, and are overdispersed.

Model

We generated synthetic crater populations for varying P (Williams et al. 2010, Williams & Pathare 2012, Williams et al., 2012). The approach is conceptually similar to that of previous studies (e.g. Popova et al., 2003), and benefits from measurements of the current Martian cratering rate (e.g., Malin et al., 2006) (see Methods) and the effects of fragmentation. We apply a geometric correction for exhumation from a cratered volume (Supplementary Material) assuming that initial crater shape is isometric over the diameter range. After bayesian fitting, we correct our P estimate for elevation (our DTMs are below datum; Mars-average P was 20% lower than local P).

We do not track secondary craters, because meter-sized endoatmospheric secondaries are likely to be braked to sub-hypervelocity speeds for the relatively thick atmospheres we are evaluating. In other words, if wet-era craters are secondaries, then early Mars' atmosphere was thin. A caveat is that the impact blast will transiently modify local *P*.

Paleopressure constraint

We compared the model to the combined dataset (DTM1+DTM2) (Figure 2). Combined best fits are P = 1640±180 mbar, falling to P = 760±70 mbar if RCM (candidate syndepositional impact craters) are also included. Because still better preservation/exposure could allow still smaller embedded craters to be uncovered, we interpret our fits as upper limits. The best fit to DTM1 embedded craters alone is 1410±250 mbar, falling to 830±90 mbar if RCM are included. The best fit to DTM2 embedded craters alone is 1770±250 mbar, falling to 710±80 mbar if RCM are included.

The results are sensitive to target strength, as expected (Dundas et al., 2010). Increasing the target rock-mass strength to a hard-rock-like 6.9 MPa (Holsapple et al., 1993) increases the upper limit on *P* to >5 bars. Our work assumes weak soil-like target strength appropriate for river alluvium in an aggrading sedimentary deposit: if sediment developed bedrock-like rock-mass strength by early diagenesis, the upper limit is greatly increased. Sensitivity tests show only a minor effect of fragmentation on the results.

We do not consider crater shrinkage or expansion by crater degradation. Only shrinkage matters for the purpose of setting an upper bound on *P*: as the crater is abraded, the exposed radius must eventually vanish. We surmise that shrinkage is a small effect because impact craters are bowl-shaped (as opposed to cone-shaped), and because rims are frequently preserved.

Environmental interpretation

Our technique sets an upper limit on the density of a thick *stable* paleoatmosphere, and cannot exclude atmospheric collapse-reinflation cycles on timescales much shorter than the sedimentary basin-filling time. General Circulation Model (GCMs) predict that atmospheric collapse to form CO_2-ice sheets and subsequent reinflation might be triggered by obliquity change (e.g., Forget et

al., 2012). If sediment accumulated at 1-100 μm/yr (e.g., Kite et al., 2013b), our DTMs could integrate over ~10^6-10^8 years of sedimentation and contain many collapse-and-reinflation cycles. Therefore one interpretation of our results is that the smaller ancient craters formed while the atmosphere was collapsed, while the rivers formed during high-obliquity, thick-atmosphere intervals.

Downward revisions to CO_2's infrared opacity indicate that *any* amount of CO_2 is insufficient to warm early Mars $\overline{T}$ to the freezing point (Forget et al., 2012). Even if further work moderates this conclusion (Haberle et al., 2012), our result is an independent curb on stable CO_2/H_2O warm-wet solutions (Figure 3). However, increased CO_2 below the warm-wet threshold primes Mars climate for surface liquid water production by other relatively short-lived mechanisms, by adding to the greenhouse effect, pressure-broadening the absorption lines of other gases, suppressing evaporitic cooling (Kite et al., 2013a), and increasing atmospheric heat capacity (Segura et al., 2008).

If the small-crater limit is representative of early Mars *P*, no known mechanism allows continuous stability of surface liquid water for the 10^4-10^5 yr needed to vertically integrate the hydrosphere. This is true even with optimistic CO_2 radiative-forcing parameterizations. Transient warming by eruptions, impacts, or infrequent orbital conditions could unfreeze the surface and shallow subsurface, allowing runoff, but would not last long enough to unfreeze ground at ~1 km depth. Therefore, atmospheric models do not support $\overline{T}$ above freezing on early Mars, which has implications for sedimentary rock formation and diagenesis, groundwater hydrology, and habitability.

Synthesis of early Mars paleoatmospheric pressure

Atmospheric loss must be part of the explanation for Mars' great drying, if only because freshwater rivers cannot flow for hundreds of km when simultaneously boiling and freezing. How high *P* was, and its decay over time, are not known. The MAVEN spacecraft will measure modern loss processes.

153 Mars would have formed with ≥6-10 bars CO_2-equivalent of carbon assuming the same initial [C]
154 and [Kr] as Earth. $^{40}Ar/^{36}Ar$ and $^{129}Xe/^{132}Xe$ suggest that 90-99% of the initial atmosphere was lost
155 prior to ~4.1 Ga. Subsequent loss rates are less clear; Mars' $C/^{84}Kr$ ratio suggests P~60 mbar
156 following the Late Heavy Bombardment (Beaty et al. 2005).
157
158 Manga et al. (2012) use a volcanic bomb sag in Gusev Crater to infer $P > 120$ mbar from the bomb
159 sag's terminal velocity. This is consistent with our result. Our small-crater results are also
160 congruent with isotopic and mineralogic indicators, which generally require more assumptions
161 than the bomb sag or small-crater methods. For example, prehnite is observed on Mars (Ehlmann
162 et al., 2011) and is unstable for CO_2 mixing ratios $>2 \times 10^{-3}$ (Digel & Ghent, 1994). This implies P
163 ≲ 1 bar, but only if water at km depth was in equilibrium with the atmosphere. The composition of
164 a carbonate-rich outcrop at Gusev has been interpreted to require $P = 0.5 – 2$ bars (van Berk et al.,
165 2012) assuming that the carbonates are a solid solution in thermodynamic equilibrium. Small
166 craters have been used to constrain more recent (≲ 1 Gya) P variations (e.g. Kreslavsky, 2011).
167
168 In future, pyroclastic-blast runout length (Dufek et al., 2011) or even rainsplash (Som et al., 2012)
169 could be used to constrain Mars atmospheric paleopressure. Curiosity's landing ellipse at Gale
170 Crater is peppered by syndepositional craters, so Curiosity could validate orbital identifications of
171 embedded craters along its traverse. The 40-year-old prediction of a connection between drying
172 and atmospheric decay could be tested by applying the small-crater technique to sedimentary
173 deposits of different ages – ranging from Mawrth (the oldest known sedimentary sequence in the
174 Solar System), through Meridiani, to the relatively young Valles Marineris opal deposits. This
175 could yield a time series of constraints on early Mars atmospheric pressure, stratigraphically
176 coordinated to the sedimentary record of Mars' great drying.
177
178 **Methods.**
179 **DTM generation.** Stereo DTMs were constructed from PSP_007474_1745/ESP_024497_1745 (DTM 1, 86
180 km^2) and ESP_017548_1740/ ESP_019104_1740 (DTM 2, 108 km^2); Supplementary Figure 1 shows
181 locations and geologic context. The procedure used for DTM extraction is similar to Kirk et al. (2008).
182 MOLA Precision Experiment Data Records (PEDRs) were used as ground control points. Optimal spatial
183 resolution obtained is a function of HiRISE image map scale (i.e., 25 cm or 50 cm) leading to 1 – 2.5

m/post DTM. Vertical precision is ~0.3 m, with a 90% probability of precision < 1 m (see Supplementary Material for details).

Cratering model. We build a synthetic impactor population by drawing randomly from the size distribution of Brown et al. (2002) and the initial-velocity distribution of Davis (1993), with an entry angle distribution that peaks at 45° (Love and Brownlee, 1991). Each population contains 3% irons, 29% chondrites, 33% carbonaceous chondrites, 26% cometary objects, and 9% "soft cometary" objects (following the Earth fireball observations of Ceplecha et al., 1998) with densities and ablation coefficients k_{ab} also set following Ceplecha et al. (1998). We advect these populations to the surface through atmospheres with scale height 10.7 km. The code does not track the curvature of planet, so we do not allow impactors to skip back to space. The atmosphere drains kinetic energy from the impactors via drag,

$$dv/dt = C_D \varrho_a v^2 A \qquad (1)$$

We assume a drag coefficient $C_D = 1$ across the velocity (v) and size range of interest (sensitivity tests in Supplementary Information)

and ablation,

$$dm/dt = (C_h \varrho_a v^3 A) / 2\zeta \qquad (2)$$

where A is cross-sectional area assuming spherical geometry, C_h is the heat transfer coefficient, and ζ is the heat of ablation. Fragmentation occurs when ram pressure $\varrho_a v^2$ exceeds M_{str}, disruption strength. M_{str} is set to 250 kPa; much lower or much higher values would be inconsistent with the observation that ½ of craters observed to form in the current 6 mbar Mars atmosphere are clusters (Daubar et al., unpublished work). This value is within the range reported for fireballs on Earth (Ceplecha et al., 1998), and our conclusions are insensitive to M_{str} variations within the Ceplacha et al. (1998) range. Particles braked to <500 m/s would not form hypervelocity craters and are removed from the simulation. Crater sizes are calculated using π-group scaling (Holsapple 1993), assuming target strength 65 kPa and target density 2000 kg/m^3 appropriate to cohesive desert alluvium (Holsapple and Housen 2007), and Holsapple scaling parameters $k_1 = 0.24$ and μ=0.41. Excavation efficiency decreases as 1/(v sin θ_i) where θ_i is the impact angle (Pierazzo & Melosh, 2000). Modeled smallest-crater size increases linearly from ~20 m at 1 bar to ~100 m at 5 bars, as expected from equating impactor and atmospheric-column masses (Melosh, 1989), and broadly consistent with low-elevation impacts on Earth (the column mass of Earth's sea-level atmosphere is equivalent to ~ 400 mbar on

Mars). Therefore, we linearly interpolate model output between runs at 0.125, 0.25, 0.5, 1.0, 2.0, 3.0, and 5.0 bars to obtain crater size-frequency distributions as a function of *P*.

References.

Barabash, S., et al. (2007), Martian atmospheric erosion rates, *Science* 315, 501-503.

Beaty, D.W., et al. (2005), Key science questions from the second conference on early Mars: Geologic, hydrologic, and climatic evolution and the implications for life, *Astrobiology* 5(6), 663-689.

Brown P., Spalding, R. E., ReVelle, D.O., Tagliaferri, E. & S. P. Worden (2002), The flux of small near-Earth objects colliding with the Earth. *Nature* 420:294–296.

Burr, D.M., et al. (2010), Inverted fluvial features in the Aeolis/Zephyria Plana region, Mars: Formation mechanism and initial paleodischarge estimates, (2010) *J. Geophys. Res.* 115, E07011.

Cassata, W. et al. (2012), Trapped Ar isotopes in meteorite ALH 84001 indicate Mars did not have a thick ancient atmosphere, *Earth Planet. Sci. Lett.* 221,461-465.

Ceplecha, Z., et al. (1998), Meteor phenomena and bodies, *Space Sci. Rev.* 84, 327-341.

Chappelow, J.E., & Golombek, M.P. (2010), Event and conditions that produced the iron meteorite Block Island on Mars, *J. Geophys. Res.* 115, E00F07.

Davis, P., Meteoroid impacts as seismic sources on Mars (1993), *Icarus*, 105, 469-478.

Digel, S. & Ghent, E.D. (1994) Fluid-mineral equilibria in prehnite-pumpellyite to greenschist facies metabasites near Flin Flon, Manitoba, Canada: implications for petrogenetic grids. *J. Metamorphic Geol.* 12, 467-477.

Dufek, J., Telling, J., & Manga, M. (2011), Multiphase Explosions on Mars: Numerical Studies of Phreatomagmatic Blast Dynamics, *42nd Lunar and Planetary Science Conference*, abstract #2237.

Dundas, C.M., Keszthelyi, L.P., Bray, V.J., and McEwen A.S., (2010), Role of material properties in the cratering record of young platy-ridged lava on Mars, *Geophys. Res. Lett.* 37, L12203.

Ehlmann, B.L. et al. (2008), Orbital Identification of Carbonate-Bearing Rocks on Mars, *Science* 322, 1828–1832.

Ehlmann, B.L., et al. (2011), Evidence for low-grade metamorphism, hydrothermal alteration, and diagenesis on Mars from phyllosilicate mineral assemblages, *Clays and Clay Minerals* 59(4), 359-377.

Forget, F., et al. (2012), 3D modelling of the early Martian Climate under a denser CO2 atmosphere: Temperatures and CO_2 ice clouds, *Icarus* 222, 81-99.

Haberle, R.M., et al. (2012), A cloud greenhouse effect on Mars: Significant climate change in the recent past?, *Mars Climate Workshop 2012*, Ames Research Center, Moffett Field.

Herrick, R.R., Sharpton, V.L., Malin, M.C., Lyons, S.N., and Feely, K. (1997), Morphology and Morphometry of Impact Craters, in *Venus II*, U. of Arizona Press, eds. S. W. Bougher, D. M. Hunten, and

R. J. Phillips, pp. 1015-1046) (catalogue as v3. Updated by R.R. Herrick in http://www.lpi.usra.edu/resources/vc/vchome.html)

Holsapple, K.A. (1993), The scaling of impact processes in planetary sciences, *Ann. Rev. Earth Planet. Sci.* 21, 333-373.

Holsapple, K.A., and Housen K.R. (2007), A crater and its ejecta: An interpretation of Deep Impact, *Icarus* 191(2:Supplement), 586-597.

Kirk, R.L., et al. (2008), Ultrahigh resolution topographic mapping of Mars with MRO HiRISE stereo images: Meter-scale slopes of candidate Phoenix landing sites, *J. Geophys. Res.* 113, E12, E00A24.

Kite, E.S., Halevy, I., Kahre, M.A., Wolff, M.J., Manga, M. (2013a), Seasonal melting and the formation of sedimentary rocks on Mars, with predictions for the Gale Crater mound, *Icarus* 223, 181-210.

Kite, E.S., Lucas, A.S., and Fassett, C.I. (2013b), Pacing Early Mars fluvial activity at Aeolis Dorsa: Implications for Mars Science Laboratory observations at Gale Crater and Aeolis Mons, moderate revisions requested by Icarus, arxiv http://arxiv.org/abs/1207.6726

Love, S.G. & Brownlee D.E. (1991), Heating and thermal transformation of micrometeoroids entering the Earth's atmosphere, *Icarus* 89, 26-43, 1991.

Malin, M. (2006), Present-Day Impact Cratering Rate and Contemporary Gully Activity on Mars, *Science* 314, 1573-1577.

Manga, M., A. Patel, J. Dufek and E.S. Kite (2012) Wet surface and dense atmosphere on early Mars inferred form the bomb sag at Home Plate, Mars, *Geophys. Res. Lett.* 39, L01202, doi:10.1029/2011GL050192.

Manning, C.V., McKay, C.P., and Zahnle, K.J. (2006), Thick and thin models of the evolution of carbon dioxide on Mars, *Icarus* 180, 38-59.

Melosh, H.J. (1989), *Impact cratering: A geologic process*, Oxford University Press.

Kreslavsky, M. A. (2011), Observational Constraints on atmospheric Pressure on Mars in the Amazonian, *Fourth International Workshop on the Mars Atmosphere: Modelling and observation*, Paris, France.

Pierazzo, E., & H.J. Melosh (2000), Understanding oblique impacts from experiments, observations, and modeling, *Annu. Rev. Earth Planet. Sci.* 28, 141-168.

Pollack, J.B., Kasting, J.F., Richardson, S.M., & Poliakoff, K. (1987), The case for a wet, warm climate on early Mars, *Icarus* 71, 203-224.

Popova, O., Nemtchinov, I., & Hartmann, W.K. (2003), Bolides in the present and past martian atmosphere and effects on cratering processes, *Meteor. & Planet. Sci.* 36, 905-925.

Segura, T.L., Toon, O.B., Colaprete, A. (2008), Modeling the environmental effects of moderate-sized impacts on Mars, *J. Geophys. Res.* 113, E11007.

Som S., Catling D., Harnmeijer J., Polivka P., & Buick R. (2012), Air density 2.7 billion years ago limited to less than twice present levels by fossil raindrop imprints. *Nature* 484, 359 - 362, 2012.

Tian, F., et al. (2010), Photochemical and climate consequences of sulfur outgassing on early Mars, *Earth & Planet. Sci. Lett.*, 295, 412-418.

van Berk, W., Fu, Y., Ilger, J.-M. (2012), Reproducing early Martian atmospheric carbon dioxide partial pressure by modeling the formation of Mg-Fe-Ca carbonate identified in the Comanche rock outcrops on Mars, *J. Geophys. Res.* 117, E10, E10008.

Vasavada, A.R., Milavec, T.J., and Paige, D.A. (1993), Microcraters on Mars: Evidence for Past Climate Variations, *J. Geophys. Res.* 98, 3469-3476.

Williams, J.-P., Aharonson, O., & Pathare, A.V. (2010), The production of small primary craters on Mars, in 41st *Lunar Planet. Sci. Conf.*, 2574.

Williams, J.-P., & Pathare, A.V. (2012), Scaling effective diameters of small impact crater clusters on Mars, in 43rd *Lunar Planet. Sci. Conf*, #2881

Williams, J.-P., Pathare, A., and Aharonson, O. (2012), Modeling small impact populations on Mars, EPSC abstracts, vol 7, EPSC2012-95, 2012.

Wood, C.A., et al. (2010), Impact craters on Titan, *Icarus* 206, 344-344.

Author contributions

E.S.K. designed research, picked craters, carried out the data-model comparison, and drafted the main text. J.-P.W. wrote the model. A.L. built the digital terrain models and wrote the corresponding Supplementary text. O.A. supervised research. All authors contributed to the interpretation of the results and to the revisions.

Acknowledgements. We thank Joe Dufek, Bethany Ehlmann, Woody Fischer, Itay Halevy, Kevin Lewis, Michael Manga, and Melissa Rice for discussions. This work was funded by an O.K. Earl Fellowship (to E.S.K.) and NASA grants NNX11AF51G (to O.A.) and NNX11AQ64G (to J.-P.W.)

Figures.

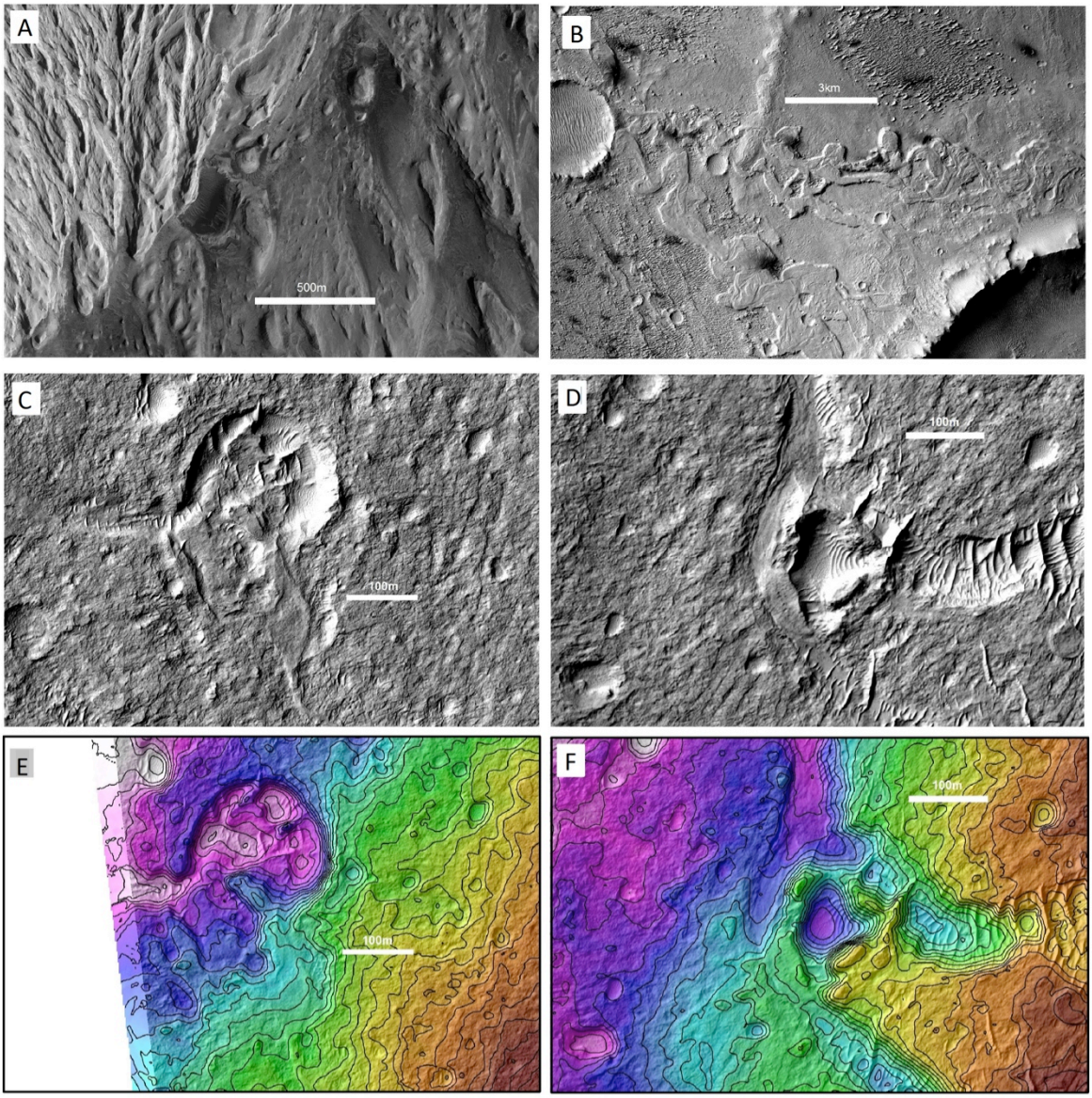

Figure 1. Gallery of ancient Martian craters. a) Crater being exhumed from beneath an unconformity within Gale Crater's mound (Aeolis Mons). ESP_019988_1750. b) Craters with fresh-appearing ejecta being exhumed from beneath meander belts, Aeolis Dorsa, P15_006973_1742_XI _05S205W; Burr et al., 2010. c) Crater being exhumed from beneath fluvial channel deposit, Aeolis Dorsa. 238 m diameter. ESP_019104_1740. d) Crater draped by fluvial channel deposit, Aeolis Dorsa, ESP_019104_1740. 141m diameter. e) Crater from (c), but with 1m elevation contours from DTM2 (see text). f) Crater from (d), with 1m contours from DTM2. (After Kite et al., 2013b).

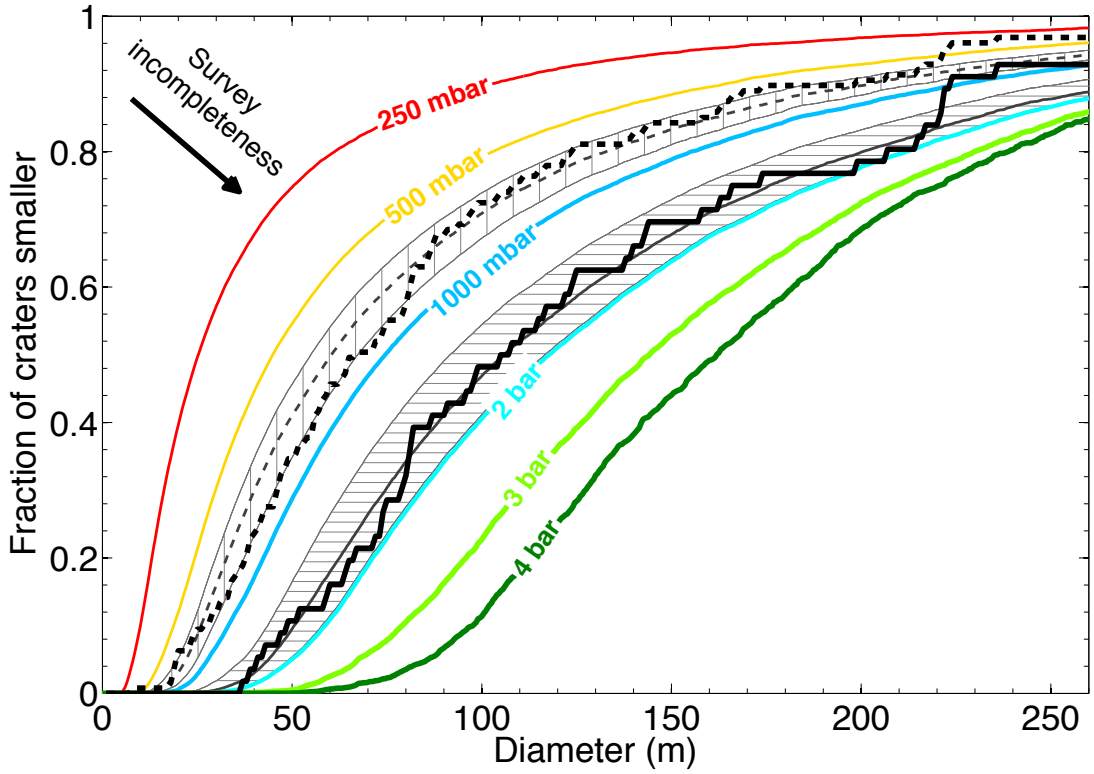

Figure 2. Upper limits on Early Mars atmospheric pressure: comparison of model crater size-frequency distributions to observations. The cumulative size frequency distributions of model exhumed-crater populations (colored lines) and observations (black lines) are shown. Solid black line corresponds to definite embedded craters. Dashed black line additionally includes rimmed circular mesas. The stair-stepping in the data curves correspond to individual craters. Gray hachured regions correspond to 2σ statistical-error envelope around the best-fit paleopressure to the datasets (which is shown by thick gray lines). Because survey incompleteness leads to an overestimate of median crater size, the best fits are upper limits.

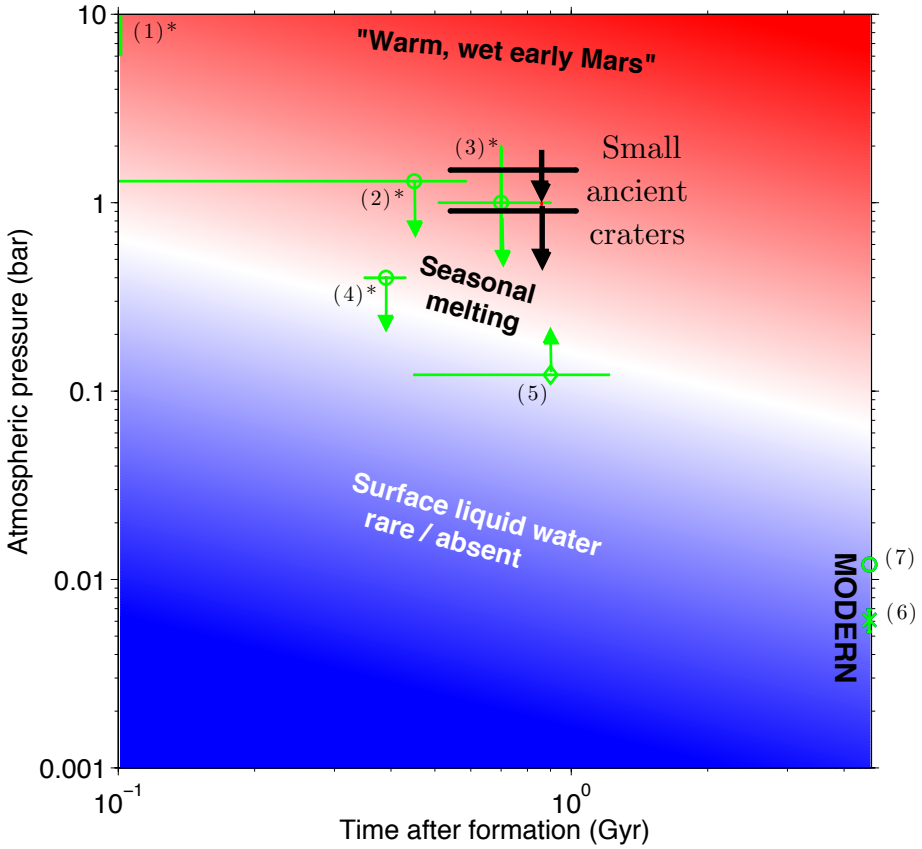

Figure 3. Paleopressure constraints on the great drying of Mars. Black symbols show the upper limit from small-ancient-craters described here, and green symbols are other estimates discussed in the text (asterisks mark indirect estimates):- (1*) initial cosmochemical estimate; (2*) prehnite stability; (3*) carbonate Mg/Ca/Fe; (4*) $^{40}Ar/^{36}Ar$ (Cassata et al., 2012); (5) bomb sag; (6) modern seasonal range; (7) modern seasonal range + observed buried South Polar CO_2 ice. Implications for sustained surface habitability are shown by background colors, from blue for too cold for melting to red for melting year-round. These are approximate and model-dependent, for example the snowmelt threshold is sensitive to assumed snowpack thermal inertia. Melting is much more difficult under the faint young Sun. "Warm, wet early Mars" refers to the long-term stable climate solution of Pollack et al. (1987). Age limits are based on geologic relations, published crater counts, and a radiogenic date for ALH 84001, except for the data added in this paper (age constraints explained in Supplementary Material.)

Supplementary Material.

Contents: Supplementary Text, Supplementary Table 1, Supplementary Figures 1-4.

1. Geologic Constraints and Geologic Context

1a. Stratigraphic Control

Stratigraphic relations prove that our DTMs sample near the center of a thick interval of fluvial deposition, and do not represent the final gasp of large-river activity. The most recent published map covering Aeolis Dorsa is Zimbelman & Schiedt (2012). Our DTMs straddle the contact of two fluvial units that fall in the area mapped by Zimbelman & Scheidt as "AHml1" (Supplementary Figure 1). These units are traceable for >300 km. The lower of the two units, which we term F1 (Fluvial 1) is defined by broad meander- belts, often with multiple preserved generations of cutoff and/or cut-and-fill. Material laterally adjacent to channel belts erodes to form yardangs, leaving the meander-belts as locally high-standing features. F1 is overlain, apparently conformably, by F2 (Fluvial 2). Our DTMs overlie this contact. F2 is a slope-forming unit, densely peppered with rimless craters, interpreted as impact craters. Across Aeolis Dorsa, F2's crater density is higher than that of the units which envelop it, especially near the contact with F1. In Context Camera (CTX) images, F2 is generally darker in tone than adjacent units. F2 is associated with modern aeolian bedform, and we interpret the sediment source for these bedforms to be erosion of F2. The erosional expression of channels in F2 is variable, but relative to channels in F1 they are typically narrower, have more frequent confluences, form more tree-like as opposed to subparallel networks, and are more frequently preserved in negative relief than are channels in F1. F2 is >100m thick and is overlain by additional fluvial units (not exposed in our DTMs) that feature channel belts wider than those in F2. In all cases, channels show little relationship to the modern topography and are eroding out of the rock: F2 channels postdate F1 channels. The base of F1 is not exposed near our study region but it is at least tens of meters below the F1-F2 contact. The total stratigraphic interval over which fluvial deposits are abundant in Aeolis Dorsa is >300m.

The simplest interpretation of the interfluve terrain in both F1 and F2 is as the overbank deposits of the rivers, but other interpretations are possible. For example, the river deposits could be the fill of incised valleys that postdate the interfluves. Several small craters are crosscut or overlain by river deposits, and the frequency of these crosscuts seems roughly consistent with the hypothesis that many or all of the ancient craters predate the horizontally adjacent river channels and channel-fill deposits (we have not attempted to verify this by Monte Carlo simulations).

1b. Age Control

The craters date from around the time when large rivers flowed on the surface of Mars; they are almost certainly pre-Amazonian, and probably Early Hesperian or older. We carried out a CTX crater count over an 8 x 10^4 km^2 region largely conterminous with Aeolis Dorsa, dividing craters > 1km into postfluvial, synfluvial/prefluvial, and undetermined on the basis of local crosscutting relationships. $N(1)$ is 1049±113 for postfluvial craters and 2049±158 for postfluvial+undetermined craters. $N(2)$ is 415±71 for postfluvial craters and 634±88 for postfluvial+undetermined craters. $N(5)$ is 37±21 for postfluvial craters, and there are no undetermined craters in this size class. Based on crater morphology we think most of the 'undetermined' craters are in fact postfluvial, implying a $N(1)$ Crater-Retention Age (CRA) on the Hesperian/Amazonian boundary and an $N(2)$ CRA straddling the Late Hesperian/Early Hesperian boundary (Werner & Tanaka, 2011). Stratigraphic relations (Zimbelman & Scheidt, 2012), and evidence in the form of mesas for removal of several hundreds of meters of overburden further support our inference that the rivers flowed in the Hesperian or Noachian. Our DTMs lie within a region of Aeolis Dorsa that has an unusually low $N(1)$: if this results from relatively rapid exhumation, consistent with the excellent preservation state of the ancient rivers, a resurfacing rate of ~1 μm/yr is implied over $10^{8\text{-}9}$ yr timescales. Relatively rapid modern erosion, combined with a high embedded-crater density, makes this a particularly attractive site for our procedure: rapid erosion minimizes the proportion of geologically-recent (synerosional) craters in the distribution, and thus the impact of false positives (assuming the false positive error rate is fixed). Our results are consistent with Zimbelman & Scheidt (2012), who additionally suggest that the rivers (i.e. Zimbelman & Scheidt's "AHml1") predate a topographically highstanding unit (their "Hmm") with a ~3.7 Ga CRA on the Hartmann & Neukum (2001) chronology. This relation is not certain from CTX and HiRISE observations: interpretation of the "AHml1"/"Hmm" contact is complicated by talus and by moats.

However, it is more likely than not that the rivers predate ~3.7 Ga because elsewhere in Aeolis-Zephyria Plana, the river units do stratigraphically underlie topographically higher-standing material. Regional geology as mapped by Irwin et al. (2010) implies that the rivers are not older than Late Noachian.

2. Details of Small Crater Analysis

When craters are dispersed through a 3D volume, the size-frequency distribution of exhumed craters will favor larger craters because a 2D surface cutting through the volume (i.e., the erosion surface) is more likely to intersect a big crater than a small one. This geometric correction is linear in crater size if craters of different sizes have the same shape, which is approximately true in the strength regime relevant to this paper.

Erosion may modify craters. The main defense against this is to fit the circles defining the craters only to parts of the crater edge which are well-preserved. A supplementary defence is to expand (contract) the resulting circles until they enclose only two (enclose all *except* two) of the hand-picked points on the crater rim. We then define the annulus enclosed by these minimal and maximal craters as a 'preservation-error annulus.' We found no significant difference between total errors (from resampling) including bootstrapping by sampling radii randomly from within the preservation-error annulus as opposed to total resampling errors excluding this effect. Therefore, we do not include this additional error in our final Bayesian paleopressure estimate.

We do find one cluster of large ancient craters, which may result from dispersal of secondaries in a thicker atmosphere (Popova et al., 2007). It is possible that future work might use ancient crater clusters to set a lower limit on atmospheric paleopressure.

We do not show the 'candidate' exhumed craters – which by definition are not definitely exhumed - because they may be significantly contaminated by synerosional craters. The regional $N(1)$ count is consistent with a landscape that is currently being sanded down at 1 μm/yr, which (assuming equilibrium between production and obliteration) would permit a considerable number of degraded synerosional craters to form in the modern thin atmosphere. However, we do not see many pristine (rayed, blocky, or deep) $D \sim 50$m craters, and we suspect that the balance is made up

by ‘candidate’ exhumed craters that are in fact relatively recent synerosional craters which have lost their rims. This is supported qualitatively by evidence of rapid small-crater degradation along the Opportunity traverse (Golombek et al., 2010). Some evidence for this suspicion comes from the cumulative size-frequency distribution of candidate craters. On a cumulative size-frequency plot, the zero-atmosphere slope on a pristine, stable surface is -3 for the 20-500m diameter craters of interest. This exponent is shallowed by the geometric correction for dispersal through a 3D volume (Δ = +1), by atmospheric filtering (Δ = +0 to +0.5, increasing with pressure), and by preferential preservation/detection of large craters. The size-frequency distribution of the ‘candidate’ craters is not as shallow as would be expected if all of these craters were exhumed. If we are wrong and the candidate exhumed craters are all syndepositional, our paleopressure upper bound would be lowered by a factor of ~2.

If the atmosphere was thick, only a small fraction of impactors would form craters. The expected frequency of exhumed craters D>50m is 90% of the zero-atmosphere value at 6 mbar, 5% at 1000 mbar, and 0.4% at 5 bar; larger craters are less attenuated to an extent that is itself a function of P. For a given embedded-crater density and top-of-atmosphere impactor flux, the inferred paleoaccumulation rate must be correspondingly lower to allow enough time for craters to form. The observed D>50m frequency is 40% (or 65% including rimmed circular mesas) of that obtained from extrapolating the frequency of D>300m embedded craters observed over a 2100 km^2 area (Kite et al., 2013b) down to 50m. The best fit to this ratio is $P \sim 100$ mbar, but the ratio is only a factor of ~2 greater than that expected for thicker atmospheres (0.25-5 bars).

We interpret craters mapped as ‘ancient’ that lie between the river deposits as being part of the same (buried/embedded) crater population as craters that are overlain by ancient river deposits. If this interpretation is correct, a histogram of river-crater interaction frequencies from a Monte Carlo trial should be consistent with the mapped population. But if our false positive rate is significantly higher away from the river deposits, this would show up as a reduced proportion of river-crater interactions relative to that expected by chance. For long, parallel river deposits of spacing W and crater diameter < river-deposit width, the fraction of intersections is approximately D/W. This is consistent with our mapped populations if we make the approximation $W = A/L$ where A is DTM

area and L is channel length. However, the geometry of the real river deposits is more complicated than this idealization. Therefore, to validate our interpretation, we did the following:-

(1) Mapped the outlines of all channels within the DTMs;
(2) Sprinkled random crater populations over the resulting maps, randomizing locations and bootstrapping radii from the observed populations. The number of 'definite' craters and of rimmed circular mesas is the same as in the mapped distribution. Craters 100% obscured by channel deposits were removed with replacement;
(3) Counted the number of crater-river interactions for this synthetic population (and the areas of overlap);
(4) Repeated 1,000 times.

We found that the 'preferred' crater population (dotted line in Figure 2) is in the 56th percentile of the synthetic distribution of crater-river interaction frequencies. The 'definite' crater population (solid line in Figure 2) has *more* river-crater interactions than 89% of the synthetic populations, which may indicate a higher likelihood that true embedded craters are relegated to 'candidate' status away from the river deposits. The Rimmed Circular Mesas have a lower interaction frequency than 90% of the random populations, probably because they are locally high-standing so that horizontally-adjacent river deposits have usually been eroded away. This procedure obviously cannot rule out a small contribution of false positives, but in combination with our geologic checklist (Supplementary Table 1) it validates our interpretation that ancient craters mapped as 'definite' between the river deposits do not have a significantly higher false positive rate than ancient craters mapped as 'definite' that underly river deposits.

3. Details of data-model comparison

Atmospheric pressure was found by fitting the data to cratering-model output, treating the impacts as a Poisson process (e.g. Wall & Jenkins, 2012; Aharonson et al., 2003). The prior is flat in log paleopressure. The impact size-frequency distribution is modeled as a function of atmospheric pressure and a flux parameter only. At first, we marginalized over the flux parameter, but in practice we found that we obtained almost the same results by using a single flux parameter chosen to produce the same number of craters as observed. When fitting the data to the model, the crater

diameters are binned in increments of 1m. Diameters < 10m are excluded from the fit. This excludes one RCM. Including this RCM lowers paleopressures by ~100 mbar, because such a small crater is a very improbable (although singular) event under a thick atmosphere. Our procedure is analogous to χ-squared fitting, but it is appropriate for the limit where each bin contains a small number of data.

4. DTM extraction procedure

The procedure used for DTM extraction follows that of Kirk et al. (2008) and uses the NGATE algorithm (Zhang, 2006). The HiRISE images making up the PSP_007474_1745-ESP_024497_1745 steropair have emission angle of 4.5 degrees and 30 degrees respectively, and a map scale of 25cm/pixel and 50cm/pixel respectively. The coarser image (ESP_024497_1745 in this case) controls the optimal spatial resolution for the topographic extraction, so we derived a 2.5 m/post DTM for this pair (DTM1). MOLA PEDRs were used as ground control points, with vertical accuracy set to 10 m, as the area contains mostly flat smooth features, for which it is difficult to link PEDR shots to surface features observed as HiRISE scale. In addition, we generated our own gridded MOLA DTM (from PEDR), which we used as a seed for extraction. The process for DTM2 was very similar.

We used several metrics for DTM validation and quality assessment. These included the LE90 (i.e., Linear Error of 90%). This value is automatically computed (i.e., by the SOCET SET photogrammetry software) as the error in elevation of one point with respect to another point within the DTM at 90% probability. In our DTM, the mean LE90 is 1.07 m and when correlation had succeeded, the highest value is 3 m. These values should be compared with the theoretical limit on vertical precision using the standard photogrammetry equation (Kirk et al., 2008):

$$EP = r\, s\, /\, (b/h)$$

Where *EP* is the expected vertical precision, *r* is the accuracy with which features can be matched (i.e., *r=0.3*), s the ground sample distance (i.e., *s = 50* cm), and the *b/h* ratio describes the convergence geometry of the stereo pair (i.e., b/h ~ 0.5). Respective values give *EP* ~ 0.3 m. The shaded relief was compared to the orthophoto using the same illumination geometry over a

constant albedo area (Figure S2 shows the comparison between the 25cm/pixel image and the DTM). The Figure S3 presents cross-sections over both the HiRISE image and the shaded relief computed from the DTM. A good match is obtained.

Supplementary References.

Aharonson, O., Schorghofer, N., & Gerstell, M.F. (2003), Slope streak formation and dust deposition rates on Mars, J. Geophys. Res. 108(E12) 5138.

Golombek, M., et al., 2010, Constraints on ripple migration at Meridiani Planum from Opportunity and HiRISE observations of fresh craters: Journal of Geophysical Research, Planets, v. 115, E00F08, doi:10.1029/2010JE003628.

Hartmann, W.K. & Neukum, G. (2001), Cratering Chronology and the Evolution of Mars, *Space Sci. Rev.* 96, 165-194

Irwin, R.P., & Watters, T.R. (2010), Geology of the Martian crustal dichotomy boundary: Age, modifications, and implications for modeling efforts*, J. Geophys. Res.* 115, E11006.

Popova, O.P., et al. (2007), Crater clusters on Mars: Shedding light on martian ejecta launch conditions, *Icarus* 190, 50-73.

Wall, J.V. & Jenkins, C.R. (2012), Practical statistics for astronomers, 2nd Edition (Cambridge Observing Handbooks for Research Astronomers), Cambridge University Press.

Werner, S.C. & Tanaka, K.L. (2011), Redefinition of the crater-density and absolute-age boundaries for the chronostratigraphic system of Mars. *Icarus* 215, 603-607.

Zhang, B. (2006), Towards a higher level of automation in softcopy photogrammetry: NGATE and LIDAR processing in SOCET SET®, paper presented at GeoCue Corporation 2nd Annual Technical Exchange Conference, Nashville, Tenn., 26–27 September.

Zimbelman, J.R., & Scheidt, S.P. (2012), Hesperian age for Western Medusae Fossae Formation, Mars. *Science* 336, 1683.

Supplementary Table 1: Checklist for identifying embedded craters.

Checklist for accepting embedded craters

Must be an impact structure that is embedded within the stratigraphy.

- Crater, or crater rim (if preserved), or ejecta (if preserved) are crosscut by fluvial deposits → accept
- Crater, or crater rim (if preserved), or ejecta (if preserved) are crosscut by fluvial channels → accept
- Crater partly overlain by sediments topographically, stratigraphically or texturally continuous with surrounding layered sediments → accept
- Crater forms a rimmed circular mesa
- Crater forms a rimmed circular mesa with flat or inward-dipping strata inside the rim; these strata need not be continuous with sediment outside (and usually are not)

Other checks:

- At same or similar level and spatially adjacent to an embedded crater; has the same preservation style (e.g., layered circular mesa) as that embedded crater
- Crater is close to circular (ellipticity < 1.15)

- Rim or edge preserved topographically in DTM over at least 180 degrees of arc (does not have to be continuous)

or

- Crater appears to be concave-up in anaglyph

if neither:

- Reject.

Ensemble checks:

- Is the same preservation style of craters found beyond the mapped background geologic unit in this geologic region? (If so, could be a younger mantling unit: reject all craters)

- Are the ellipticities aligned?
- Is the distribution of crater centers random in space?
- Do any clusters match to geology? (If so, suspect soft-sediment deformation).

Checklist for rejecting ancient craters: rejects override accepts

Either not clearly an impact structure, or not embedded within stratigraphy

- Rim preserved mostly (>2/3) intact, and rim ellipticity > 1.5 → immediate reject
- Crater (and ejecta, if visible) are not superposed by anything other than active/recently active bedforms → immediate reject
- Rays visible → immediate reject
- Crater could be a prolongation of nearby deformation pattern with cell-shaped sediments and upcurled edges ('spatulate' soft-sediment deformation).
- (For circular mesas) The height of the mesa exceeds the radius of the flat top or rim by >1.5 (risk of being a rootless cone or explosion pit analogous to von Braun/Goddard at the Spirit landing site).
- There is a rim visible around all or most of the top of the structure, but the elevation of the rim is much lower on one side of the structure (immediate reject; suggestive of volcanism or soft-sediment deformation)

Ensemble level checks for circular mesas - Is there a connection between the relief of the mesa and the diameter of the depression on top? if yes, argues for explosive cone rather than eroded/exhumed impact crater.

557

Supplementary Figures.

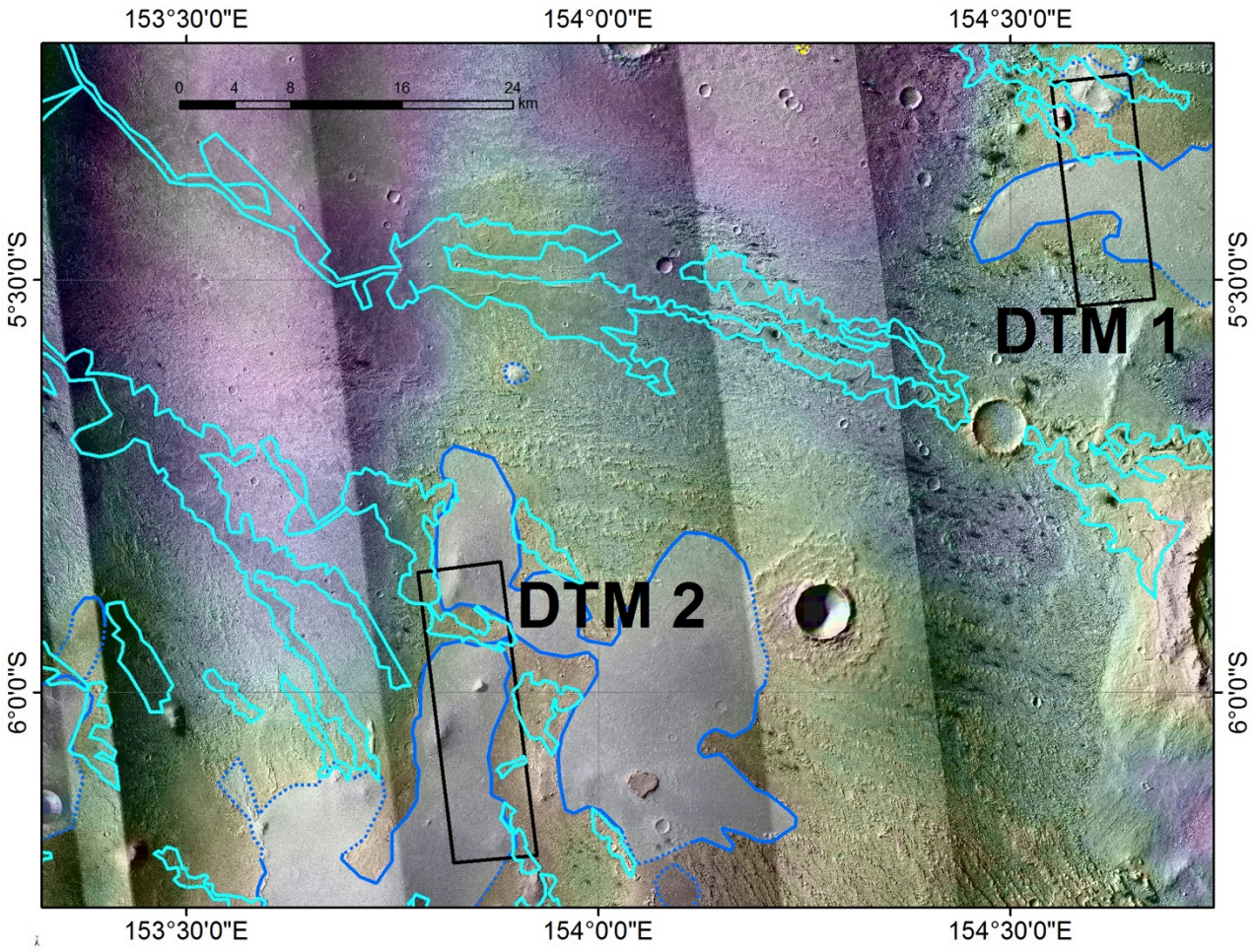

Supplementary Figure 1. Geologic context of DTMs. Topographically lower fluvial unit ("F1", no tint) contains large meander belts (cyan outlines). Topographically higher fluvial unit ("F2", white tint) contains many river deposits but lacks large meander belts. F1/F2 contact is shown as a solid blue line where mapped with high confidence, and as a dotted blue line where inferred. Background color is cued to MOLA topography (range ~ 500m).

Supplementary Figure 2.

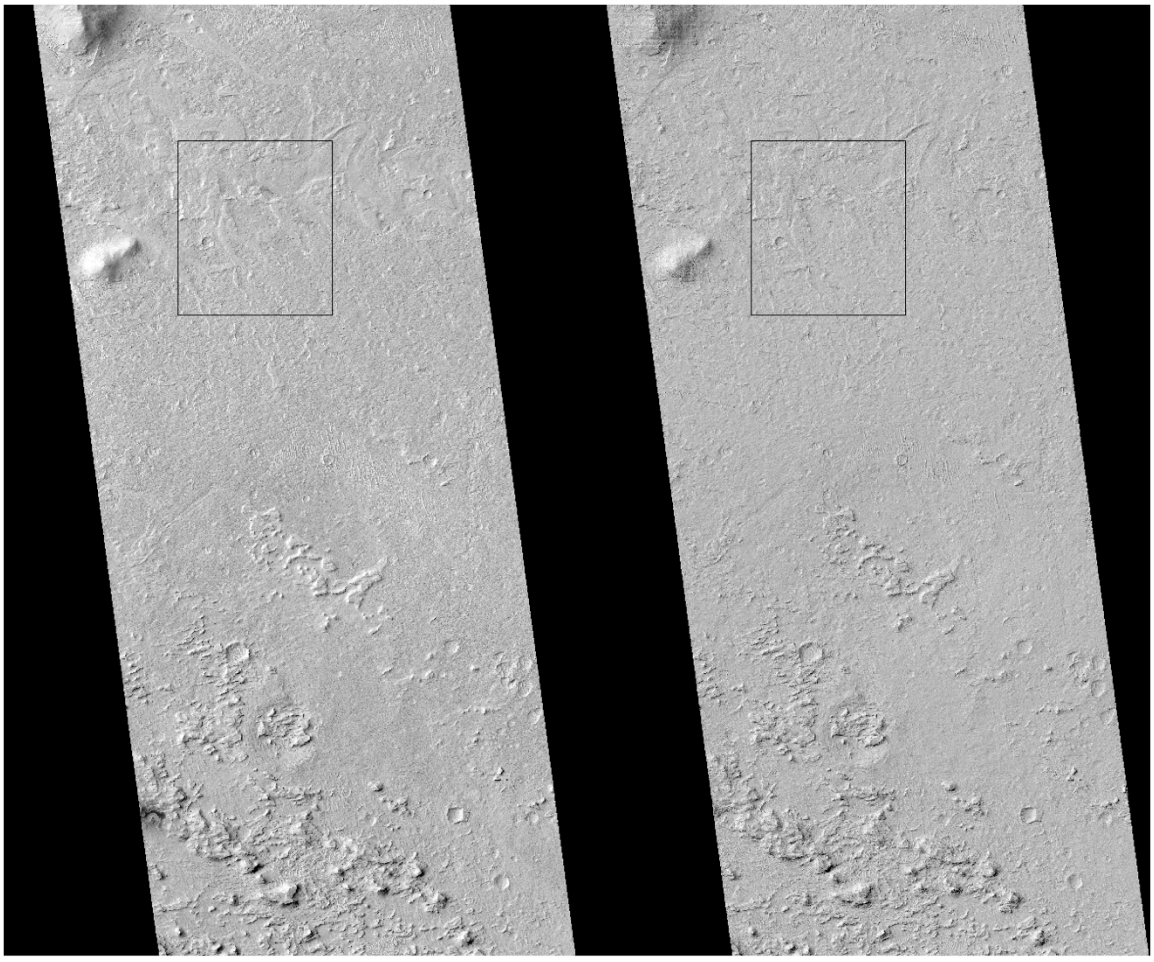

Supplementary Figure 2. PSP_007474_1745 image on left, shaded relief of corresponding DTM (DTM1, PSP_007474_1745/ESP_024497_1745) on right illuminated using the same illumination geometry. Black box shows region highlighted in Supplementary Figure 3.

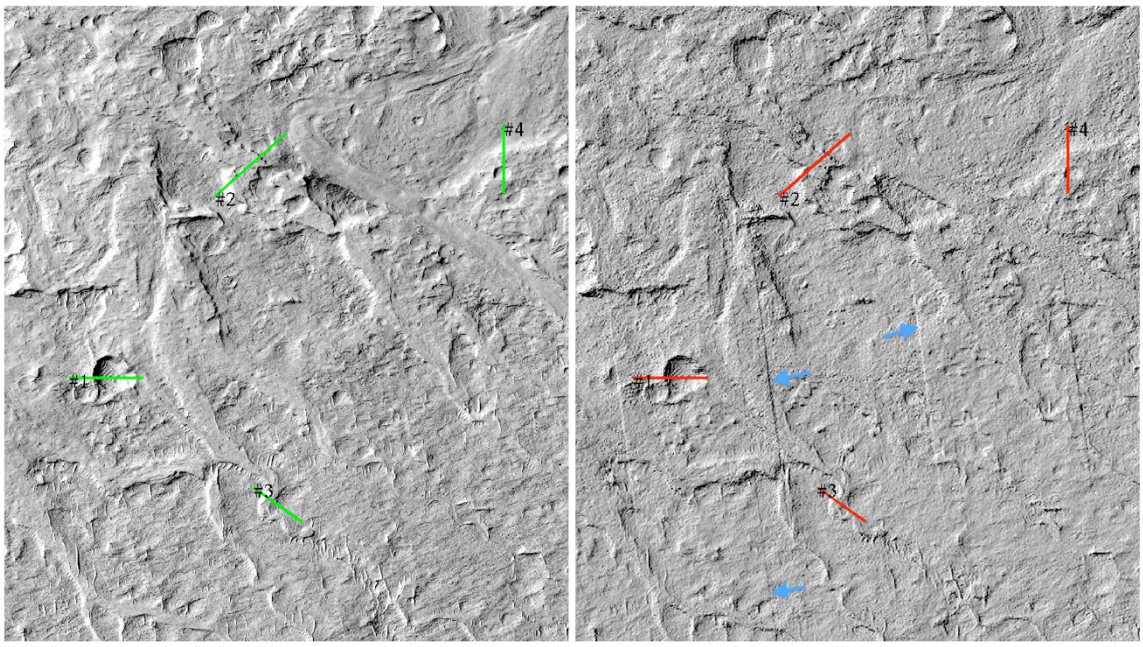

Supplementary Figure 3. Comparison between HiRISE image and the stereo DTM. (left) PSP_007474_1745 image (25cm/pixel) - (right) shaded relief from the stereo extraction. Seams at the boundaries between HiRISE CCDs are visible in the DTM (blue arrows on right panel). Their obvious presence makes it possible to take them into account in any measurement. The red and green profiles correspond to the cross-sections shown on Supplementary Figure 4.

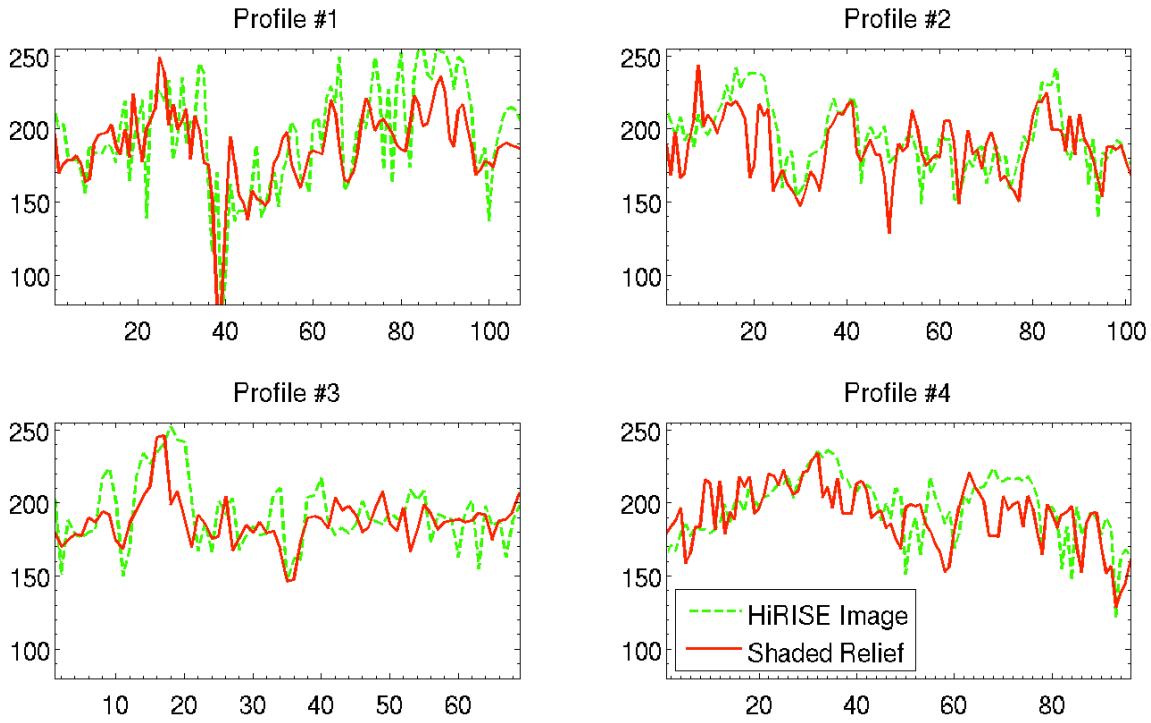

Supplementary Figure 4. Cross-sections along both HiRISE image (green) and DTM shaded relief (red) computed using the actual illumination geometry. A good agreement is obtained at the DTM post resolution, highlighting the good quality of this DTM extraction.